Rare Met.
https://doi.org/10.1007/s12598-022-02207-7

RARE METALS

MINI REVIEW

New insights on $(V_{10}O_{28})^{6-}$-based electrode materials for energy storage: a brief review

Tao Zhou, Ling-Ling Xie, Yu Niu, Hao-Ran Xiao, Yu-Jie Li, Qing Han, Xue-Jing Qiu, Xin-Li Yang, Xian-Yong Wu*, Li-Min Zhu*, Huan Pang*, Xiao-Yu Cao*

Received: 30 June 2022 / Revised: 20 July 2022 / Accepted: 25 July 2022

Abstract Progress in humanity has intensified the demand for efficient and renewable energy storage, which warrants the development of advanced rechargeable batteries such as lithium-ion batteries (LIBs), sodium-ion batteries (SIBs), zinc-ion batteries (ZIBs), and lithium-sulfur batteries (Li–S batteries). Nevertheless, these batteries still suffer from certain limitations, such as the insufficient capacity and inferior stability in their electrode materials. Therefore, developing a feasible electrode material for Li/Na/Zn ion storage represents a critical challenge. Recently, polyoxovanadates (POVs) materials, particularly decavanadate anion $(V_{10}O_{28})^{6-}$ clusters, have attracted considerate attention as promising battery electrodes, due to their rich multi-electron redox process, high structural stability, simple preparation process, and abundant ligand environment. In this review, we provide an overview of the research progress of $(V_{10}O_{28})^{6-}$-based materials in various metal-ion battery systems, including LIBs, SIBs, ZIBs, and Li–S batteries. We also discuss the underlying challenges associated with this type of materials, and we provide alternative strategies to overcome these issues. This review aims to facilitate the research and development of the next-generation $(V_{10}O_{28})^{6-}$-based battery materials.

Keywords $(V_{10}O_{28})^{6-}$; Electrode materials; Batteries; Energy storage; Progress and perspective

1 Introduction

To efficiently utilize the clean energy resources such as wind, solar, and tidal, various energy storage technologies have been actively studied and developed [1–6]. Among them, rechargeable batteries stand out as the prime choice for portable electronics, electric vehicles, and stationary energy storage systems, due to their high energy density, reliable performance, and low maintenance cost [7–12]. Presently, battery research is concentrated on lithium-ion batteries (LIBs), sodium-ion batteries (SIBs), zinc-ion batteries (ZIBs), potassium-ion batteries (KIBs), and lithium-sulfur batteries (Li–S batteries) [13–19]. Taking the typical SIBs as an example, with the advantages of abundant resources and wide distribution of Na elements,

T. Zhou, Y. Niu, H.-R. Xiao, Y.-J. Li, Q. Han, X.-L. Yang, L.-M. Zhu*, X.-Y. Cao*
School of Chemistry and Chemical Engineering, Henan University of Technology, Zhengzhou 450001, China
e-mail: lmzhu@haut.edu.cn

X.-Y. Cao
e-mail: ca@haut.edu.cn

T. Zhou, L.-L. Xie, Y. Niu, H.-R. Xiao, Y.-J. Li, Q. Han, X.-J. Qiu, X.-L. Yang, X.-Y. Cao
Key Laboratory of High Specific Energy Materials for Electrochemical Power Sources of Zhengzhou City, Zhengzhou 450001, China

L.-L. Xie, X.-J. Qiu
School of Environmental Engineering, Henan University of Technology, Zhengzhou 450001, China

X.-Y. Wu*
Department of Chemistry, University of Puerto Rico-Rio Piedras Campus, San Juan, PR 00925, USA
e-mail: xianyongwu2020@gmail.com

L.-M. Zhu, H. Pang*
School of Chemistry and Chemical Engineering, Yangzhou University, Yangzhou 225009, China
e-mail: panghuan@yzu.edu.cn

Published online: 10 February 2023

SIBs have been considered a competitive candidate to replace traditional LIBs for large-scale energy storage [20–22]. Similarly, other metal-ion batteries such as zinc and potassium have also been developed extensively, due to the high abundance of these elements. As a rule, a battery system usually consists of three main components: cathode, anode, and electrolyte. Compared with electrolytes, much more research efforts are devoted to the electrode material level [23–26]. However, the contemporary electrode materials still exhibit inferior performance in short-term and long-term cycling, possibly due to the intrinsic defects of them [27–29]. Furthermore, many electrodes that manifest fast capacity decay can be assigned to the irreversible structural changes during the ion insertion/extraction process [30, 31]. Therefore, it is of crucial importance to rationally design suitable electrode materials for high-performance batteries [23, 32, 33].

Except for traditional electrode materials, polyoxometalates (POMs) have started to attract attention in recent years by their ability to be activated in conjunction with conductive materials. As a result, battery research based on POMs materials is coming into the public view. Notably, POMs can remarkably change the electronic structure of clusters and thus affect the electrochemical performance of batteries [34, 35]. Polyoxovanadates (POVs), a typical branch of POMs, can construct all sorts of cluster structures based on different valence states of vanadium (+ 2, + 3, + 4 and + 5). Moreover, POVs enjoy rich coordination conditions that could be achieved by adjusting experimental parameters (e.g., pH, temperature, stoichiometric ratio, time, etc.) [36]. In addition, the attractive redox properties of POVs allow for reversible multi-electron transfer processes along with a stable crystal structure [37, 38]. As one of the most investigated and well-characterized POVs, the orange decavanadate anion $(V_{10}O_{28})^{6-}$ delivers great supramolecular assembly and electrochemical properties [36]. The downside is that vanadium is toxic and faces dissolution problems during the cycle, which may limit its practical application [39].

$(V_{10}O_{28})^{6-}$ anion cluster is usually structurally stable in the acidic pH range. Structurally, ten vanadium atoms are assembled into a compact structure with a unit cell size of 0.83 nm × 0.77 nm × 0.54 nm, where V^{5+} occupies the octahedral gap of the ten [VO_6] units [40, 41]. In this mini-review, the authors focus on $(V_{10}O_{28})^{6-}$-based electrodes and introduce the very recent research progress in different battery systems. We review their electrochemical performance for different ion storage, discuss the potential challenges for future application, and propose alternative strategies to address these issues. This work provides a comprehensive overview of $(V_{10}O_{28})^{6-}$-based materials, and it will bring new inspirations of $(V_{10}O_{28})^{6-}$-based electrodes for future battery applications (Fig. 1).

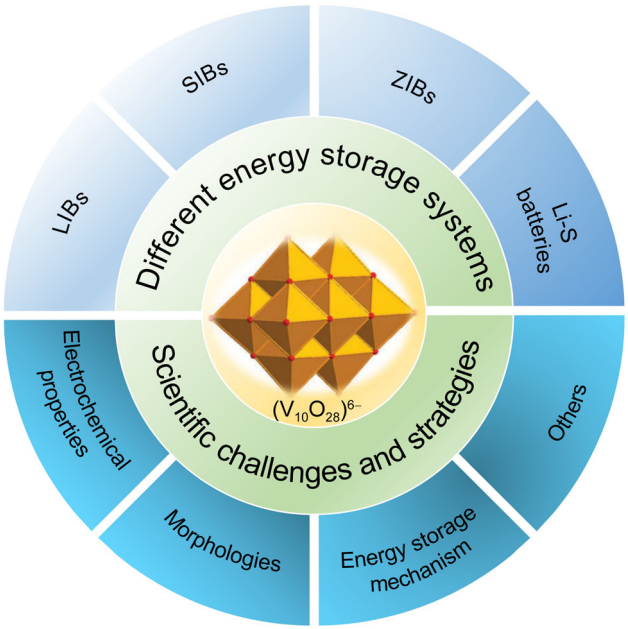

Fig. 1 Overview picture of $(V_{10}O_{28})^{6-}$-based electrode materials in energy storage batteries

2 POVs [$(V_{10}O_{28})^{6-}$-based] in different batteries

Until now, most efforts have concentrated on decavanadates anion cluster $(V_{10}O_{28})^{6-}$ in POVs [42]. These hydrated salts are typically prepared by liquid-phase modulation, that is, synthesized under aqueous conditions and then isolated out, with the chemical formula of $M_6[V_{10}O_{28}]\cdot xH_2O$ (M = Li, Na, K, etc.) [27]. The multi-electron redox capability of POVs has been highly valued lately in the battery field. In this section, the research progress of $(V_{10}O_{28})^{6-}$-based electrode materials in four systems were highlighted. Table 1 shows some of the most commonly reported $(V_{10}O_{28})^{6-}$-based electrode materials and their electrochemical properties for batteries.

2.1 $(V_{10}O_{28})^{6-}$ in LIBs

As a representative of energy storage devices, LIBs already enjoy a long history in the pursuit of electrode materials. Dating back to the past, the application of $(V_{10}O_{28})^{6-}$-based electrode materials for LIBs is slightly earlier than those employed for other ion batteries. The reported results indicated that $(V_{10}O_{28})^{6-}$-based materials present a promising future for energy storage.

Ma et al. prepared a new material, $Li_6V_{10}O_{28}$, by hydrothermal synthesis and annealing, which was derived from the dehydration of $[Li_6(H_2O)_{16}V_{10}O_{28}]_n$ [43]. Figure 2a, b displays X-ray diffraction (XRD) patterns of $[Li_6(H_2O)_{16}V_{10}O_{28}]_n$ and $Li_6V_{10}O_{28}$, reflecting the high purity orange single crystal. Besides that, the dehydrated

Table 1 Comparison of electrochemical performance of $(V_{10}O_{28})^{6-}$-based electrode materials in different battery systems

Materials	Cathode/anode	Electrolyte component	Testing voltage / V	Initial discharge capacity (discharge capacity, cycles, current density)	Battery types	Refs.
$Li_6V_{10}O_{28}$	Cathode	1 mol·L^{-1} $LiPF_6$	2.0–4.2	132 (100, 15 cycles, 0.2 mA·cm^{-2})	LIBs	[43]
$Li_6V_{10}O_{28}$	Cathode	1 mol·L^{-1} $LiPF_6$	2.0–4.2	212.4 (167.7, 30 cycles, 1.0 mA·cm^{-2})	LIBs	[44]
$Na_6[V_{10}O_{28}]$	Cathode	1 mol·L^{-1} $LiPF_6$	1.75–4.0	–	LIBs	[45]
MgV_{10}	Cathode	1 mol·L^{-1} $LiPF_6$	1.0–3.8	198.8 (180, 60 cycles, 50 mA·g^{-1})	LIBs	[46]
$KNaV_{10}$	Cathode	1 mol·L^{-1} $LiPF_6$	1.0–3.8	152.6 (–, 60 cycles, 50 mA·g^{-1})	LIBs	[46]
$Na_6[V_{10}O_{28}]$	Anode	1 mol·L^{-1} $NaClO_4$	0–3.8	> 300 (276, 10 cycles, 20 mA·g^{-1})	SIBs	[49]
KZVO	Cathode	3 mol·L^{-1} $Zn(CF_3SO_3)_2$	0.2–1.9	223.4 (218, 50 cycles, 100 mA·g^{-1})	ZIBs	[38]
$Na_6V_{10}O_{28}$	Cathode	3 mol·L^{-1} $Zn(CF_3SO_3)_2$	0.2–1.9	202.3 (169.5, 100 cycles, 100 mA·g^{-1})	ZIBs	[59]
PANI-$V_{10}O_{28}$	Cathode	8 mol·L^{-1} $ZnCl_2$	0.2–1.6	(82% capacity retention, 2000 cycles, 8 A·g^{-1})	ZIBs	[60]
NVO	Cathode	1 mol·L^{-1} LiTFSI + 2 wt% $LiNO_3$	1.7–2.8	1348 (814, 100 cycles, 0.1C)	Li–S batteries	[62]

$Li_6V_{10}O_{28}$ still maintains an orthorhombic symmetry framework structure. Figure 2c depicts three-dimensional (3D) structure space view of $Li_6V_{10}O_{28}$. Note that there is a long tunnel inside the framework structure of $Li_6V_{10}O_{28}$, which will facilitate the movement of Li^+ during the charging and discharging process. In subsequent tests, $Li_6V_{10}O_{28}$ delivered higher conductivity than $LiMn_2O_4$, $LiFePO_4$ and $LiCoO_2$ at room temperature, owing to their larger tunnel in the skeleton structure that facilitates the movement of Li^+ and electrons. To further explore the electrochemical performance, electrochemical impedance spectroscopy (EIS, Fig. 2d) and galvanostatic charge–discharge (GCD) tests were performed. As the cycle proceeded, the value of resistance (R) decreased from 317 to 26 Ω, suggesting that the $Li_6V_{10}O_{28}$/electrolyte interface was activated and gradually reached the equilibrium stability. In addition, GCD curves of the first seven cycles overlap well (Fig. 2e), indicating the excellent reaction reversibility. The initial test of $Li_6V_{10}O_{28}$ cathode in LIBs delivered a discharge capacity up to 132 mAh·g^{-1} in the voltage range between 2.0 and 4.2 V (vs. Li^+/Li) at a current density of 0.2 mA·cm^{-2}, and the capacity remains above 100 mAh·g^{-1} after 15 cycles with a high Coulombic efficiency (Fig. 2f).

Subsequently, Liu and Wang [44] synthesized the rod-shaped $Li_6V_{10}O_{28}$ powder by rheological phase reaction and conducted electrochemical tests. After sintering at different temperatures, a gradual change in the material morphology from agglomerated small particles to rod-like morphology was noted, indicating a more regularized growth with increasing sintering temperature. Interestingly, X-ray photoelectron spectroscopy (XPS) analysis demonstrated that the product consisted of a single valence vanadium atom, identified by the binding energy of V as the unique V^{5+} valence state. In the charge–discharge tests, the stability was the worst despite the highest initial discharge capacity at 450 °C. That was primarily due to the larger and longer material size as the temperature got higher. The intercalation of Li^+ during the cycle was a diffusion-controlled process, so materials with long paths slowed down the diffusion of Li^+, which resulted in a lower discharge capacity. In contrast, the material at 600 °C delivered good cycling stability, with an initial discharge capacity of 212.4 mAh·g^{-1} and a stabilized capacity at 167.7 mAh·g^{-1} after 30 cycles.

Srinivasan et al. investigated the polyoxovanadate $Na_6[V_{10}O_{28}]$ as a cathode material for LIBs, focusing on its electron transfer properties on long and short timescales [45]. The physical properties attributed to $[V_{10}O_{28}]^{6-}$ were explored by ^{51} V nuclear magnetic resonance (^{51} V NMR), and interestingly, the corresponding characteristic signals were detected at -514×10^{-6}, -500×10^{-6} and -424×10^{-6}, which represented three distinct V environments in the $[V_{10}O_{28}]^{6-}$ anion (Fig. 2g). Additionally, the authors evaluated the electron transfer of $Na_6[V_{10}O_{28}]$ by in situ V K-edge X-ray absorption near edge structure (XANES) measurements and chronoamperometric experiments (Fig. 2h, i). The former demonstrated the electronic structure information of the $[V_{10}O_{28}]^{6-}$ in fully oxidized, fully reduced, and three intermediate states. The latter explored information on the dynamic processes occurring at the electrode–electrolyte interface that follows immediately after perturbing the system from a steady-state by a potential pulse. Both sets of experiments complement each other and present a new insight into electron transfer in $Na_6[V_{10}O_{28}]$, which may be divided into three main parts:

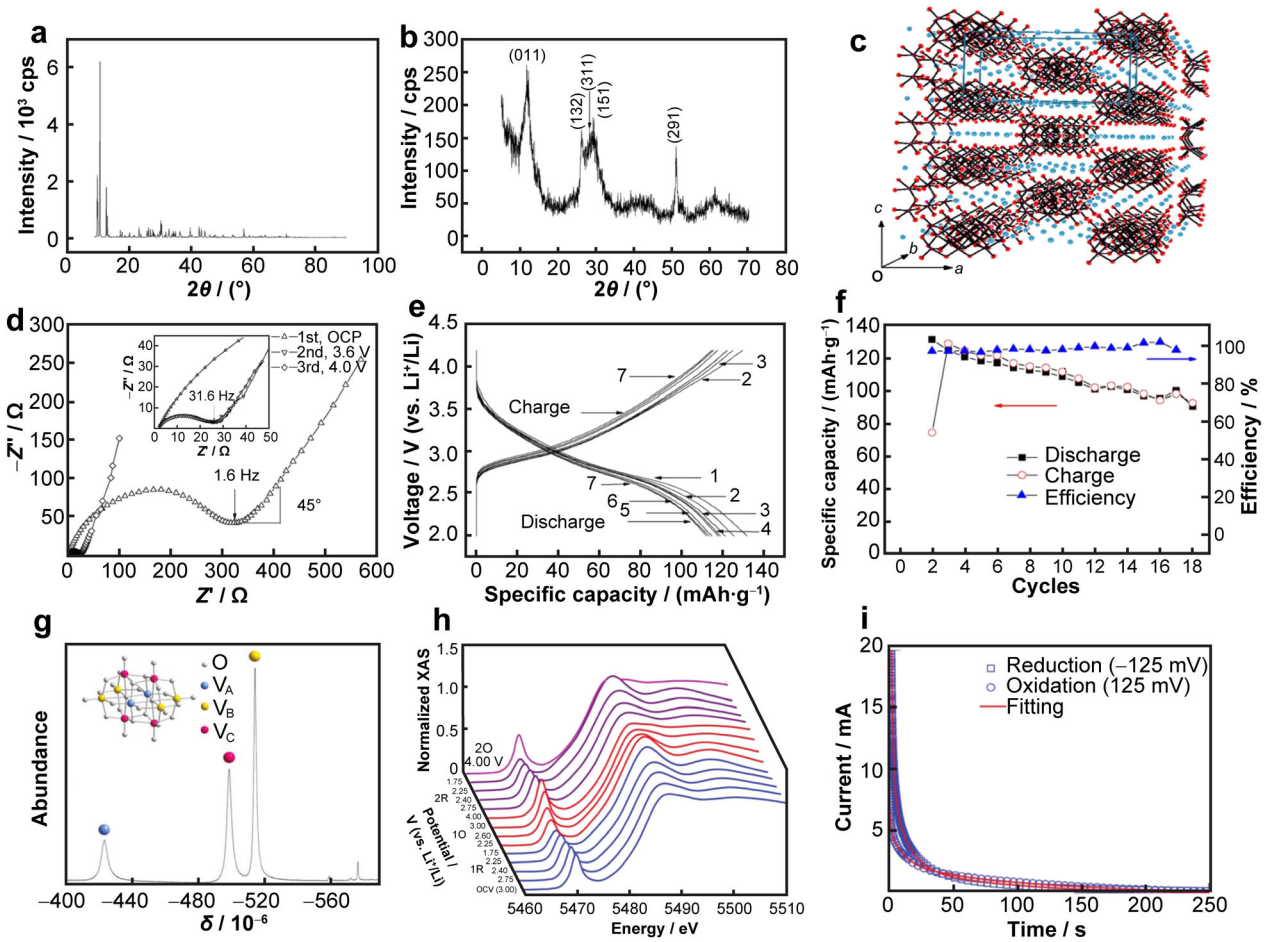

Fig. 2 XRD patterns of **a** $[Li_6(H_2O)_{16}V_{10}O_{28}]_n$ and **b** $Li_6V_{10}O_{28}$; **c** schematic diagram of 3D structure of $Li_6V_{10}O_{28}$ (blue dots being Li^+ ions); **d** Nyquist plots of EIS on $Li_6V_{10}O_{28}$ cathodes at different potentials; **e** GCD curves of $Li_6V_{10}O_{28}$ for the first seven cycles; **f** cycle performance of $Li_6V_{10}O_{28}$. Reproduced with permission from Ref. [43]. Copyright 2006, Elsevier. **g** ^{51}V NMR spectrum of $Na_6[V_{10}O_{28}]$; **h** normalized in situ V K-edge XANES spectra for redox process of $Na_6[V_{10}O_{28}]$ cathodes; **i** examples of transient currents with fitting curves at 25 °C. Reproduced with permission from Ref. [45]. Copyright 2017, The Royal Society of Chemistry

(1) V valence state in $Na_6[V_{10}O_{28}]$ can be reversibly reduced ($+5 \rightarrow +4$). (2) The electron transfer of $Na_6[V_{10}O_{28}]$ was about 30 times faster than $LiFePO_4$. (3) The fast electron transfer rate was achieved by reorganization energy smaller than $LiFePO_4$.

Considering that the insertion/extraction of Li^+ requires a stable structure, Liu et al. prepared two different polyoxovanadate materials as Li^+ storage reservoirs for investigation [46]. By optimizing the counter cations, they successfully designed an extended 3D structure where $[V_{10}O_{28}]^{6-}$ served as an "electron sponge", and theoretically, ten electrons between $[V_{10}O_{28}]^{6-}$ and $[V_{10}O_{28}]^{16-}$ were reversibly absorbed during each charge/discharge process. Taking $Mg_2(NH_4)_2V_{10}O_{28}{\cdot}nH_2O$ (MgV_{10}) with one-dimensional channels that omit water molecules as an example (Fig. 3a), the expected lithiation process of MgV_{10} materials manifested that the existence of such one-dimensional channels facilitated Li^+ migration (Fig. 3b). Thus, further physical characterization and electrochemical performance analysis were performed by selecting suitable cations (K^+, Mg^+). Figure 3c, d illustrates the experimental and simulated XRD patterns of $K_4Na_2V_{10}O_{28}{\cdot}nH_2O$ ($KNaV_{10}$) and MgV_{10}. Significantly, the characteristic diffraction peaks of the two prepared materials were consistent with the simulated data, suggesting the high purity of these compounds. Figure 3e, i presents the morphological features of the dehydrated $KNaV_{10}$ and MgV_{10}, respectively, which exhibited an interconnected, open, and porous structure composed of numerous nanosheets compared with $KNaV_{10}$ with irregular particles. Since the solubility product constants of K^+ and Na^+ surpass those of Mg^{2+}, the crystallization rate of $KNaV_{10}$ was slower than that of MgV_{10}, resulting in a massive particle shape in the former and a sheet-like morphology in the latter, which also confirmed that the different morphologies were related to the counter cation

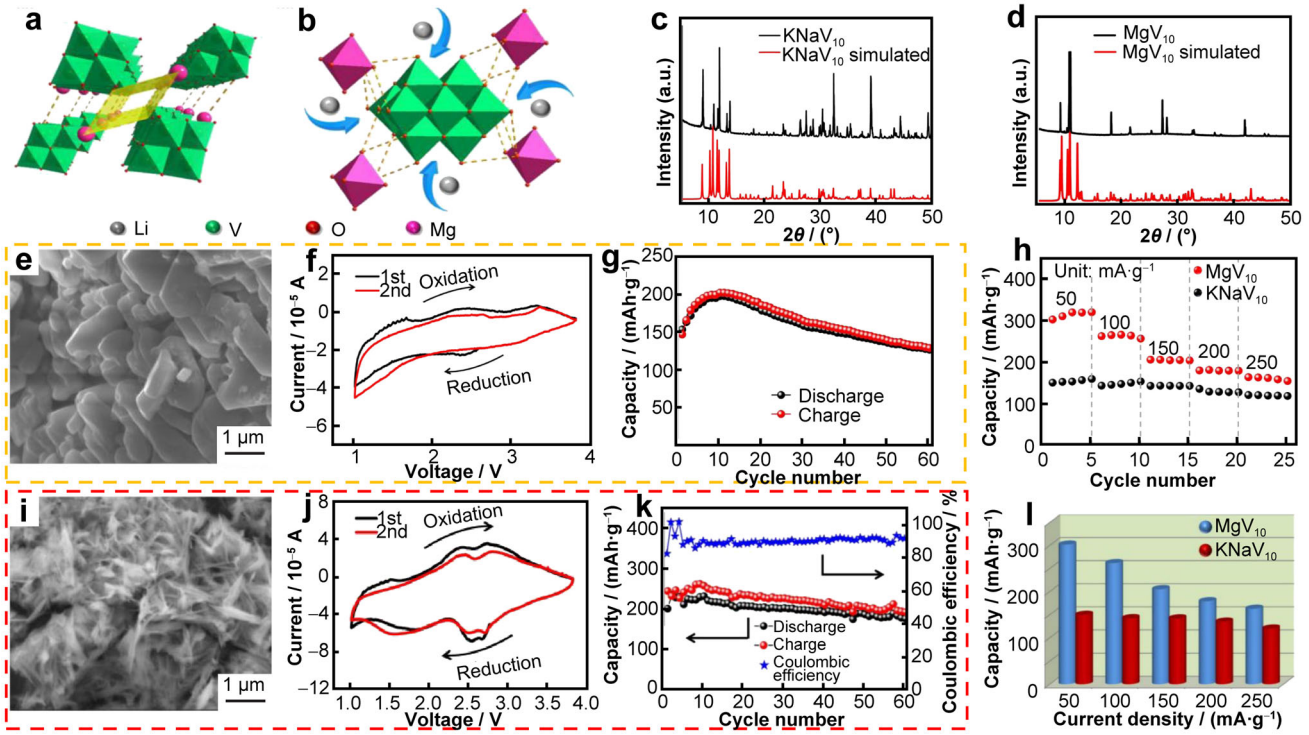

Fig. 3 Schematic crystal structure of **a** MgV_{10} and **b** expected lithiation process; experimental and simulated comparison of XRD patterns of **c** $KNaV_{10}$ and **d** MgV_{10}; **e** SEM image, **f** CV curves, **g** cycle performance of $KNaV_{10}$; **i** SEM image, **j** CV curves, **k** cycle performance of MgV_{10}; **h, l** rate performance between $KNaV_{10}$ and MgV_{10}. Reproduced with permission from Ref. [46]. Copyright 2017, The Royal Society of Chemistry

directed crystallization process [47, 48]. Moreover, MgV_{10} displayed a much better rate performance at different current densities (Fig. 3h, l), which could be ascribed to 3D interconnected, porous, and open structural characteristics. Such a significant difference between the two types of materials proved that factors such as structural stability, morphology, and regulation of counter cations collectively affected the rapid diffusion and storage of Li^+.

2.2 $(V_{10}O_{28})^{6-}$ in SIBs

To date, there are limited studies on $(V_{10}O_{28})^{6-}$-based material in SIBs. Thus, we focus on the typical $Na_6[V_{10}O_{28}]$ material and discuss its Na-storage behavior.

Similarly, Srinivasan et al. proposed a polyoxometalate $Na_6[V_{10}O_{28}]$ as a suitable anode for SIBs and conducted a series of physical characterization and electrochemical tests in 2015 [49]. $Na_6[V_{10}O_{28}]\cdot 16H_2O$ crystals were obtained by precipitating $NaVO_3$ solutions conditioned by HCl with ethanol, and the high purity of $Na_6[V_{10}O_{28}]\cdot 16H_2O$ was confirmed using ^{51}V NMR. The Fourier-transform infrared spectroscopy (FTIR) spectrum of Fig. 4a demonstrated the characteristic absorption bonds belonging to the $[V_{10}O_{28}]^{6-}$ cluster. Typical absorption peaks located at 847 and 746 cm^{-1} were attributed to the antisymmetric stretching of V–O–V, the symmetric stretching vibration of V–O–V at 521 cm^{-1}, while 956 cm^{-1} corresponded to the terminal V=O bond [50]. In addition, the specific surface area of $Na_6[V_{10}O_{28}]\cdot 16H_2O$ was calculated from N_2 isothermal adsorption and desorption curves and Brunauer–Emmett–Teller (BET) measurements as 21 $m^2\cdot g^{-1}$ (Fig. 4b). According to the pore size distribution (Fig. 4c), most pores were mesoporous between 3 and 5 nm, while the remaining pore sizes vary between ~ 5 and 160 nm. Based on field emission scanning electron microscopy (FESEM) and high resolution transmission electron microscopy (HRTEM), $Na_6[V_{10}O_{28}]\cdot 16H_2O$ presented a rod-like morphology with diameters located in the range of 0.5 − 1 μm accompanied by an aspect ratio of 5 − 10 (Fig. 4d–f). Moreover, the micro-rods are polycrystalline depending on HRTEM and display random orientation with *d*-spacing of 0.769 and 0.333 nm. By comparing cyclic voltammetry (CV) curves of electrodes with and without active materials, it can be observed that the current of the redox process involved during the first discharge was (at least partially) not caused by the redox reaction of the active material. Namely, the reaction initiated by the active material does not seem to be

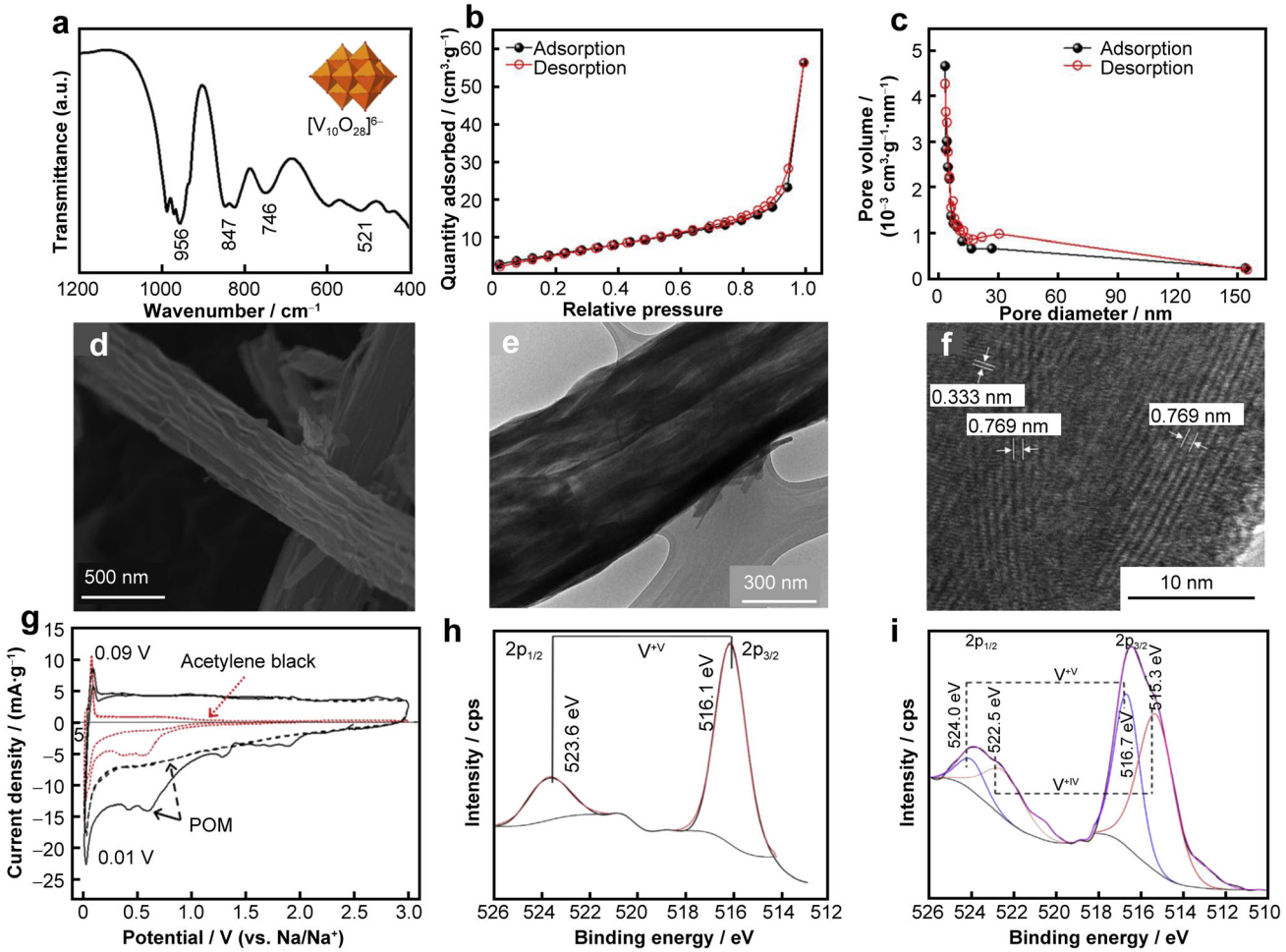

Fig. 4 **a** FTIR spectrum, **b** N_2 isothermal adsorption and desorption curves, and **c** pore size distribution of $Na_6[V_{10}O_{28}]\cdot 16H_2O$; **d** SEM image, **e** TEM image, and **f** HRTEM image of $Na_6[V_{10}O_{28}]\cdot 16H_2O$; **g** CV curves of $Na_6[V_{10}O_{28}]$ in a half-cell at 0.01 $mV\cdot s^{-1}$; **h** fine V 2p-XPS spectra of pristine and **i** discharged $Na_6[V_{10}O_{28}]$. Reproduced with permission from Ref. [49]. Copyright 2015, Elsevier

the reason for this irreversible capacity, but probably due to the partial decomposition of the electrolyte, forming a solid electrolyte interface [51, 52].

Besides that, the subsequent CV curve presented a characteristic shape similar to a supercapacitor rather than a typical intercalation process (Fig. 4g). Interestingly, a couple of small characteristic peaks were noted at 0.01 and 0.09 V, indicating the presence of a definite electrochemical process (possibly originating from acetylene black). Subsequently, XPS was utilized to detect whether the capacitive process was only physical adsorption or associated with an electrochemical redox reaction (Fig. 4h, i). In the intrinsic material, only the oxidation state of + 5 valence V was observed. However, the valence state of vanadium was partially induced to + 4 valence when discharged. Thus, these polyanions actually played the role of redox centers, allowing Na^+ to accumulate between them, while V ions were reduced to hold the charge balance. Through performance tests of half- and full-cells, this type of material has also been proven to be a suitable choice as anode for SIBs.

2.3 $(V_{10}O_{28})^{6-}$ in ZIBs

As aqueous ZIBs develop, growing attention has been paid to the search for high-energy and long-cycling cathode materials [53, 54]. Since several existing cathode materials suffer from corresponding defects, the pursuit of suitable novel cathodes is highly desired [55, 56]. Due to their appealing properties, $(V_{10}O_{28})^{6-}$ materials also find applications in ZIBs.

More recently, Cao et al. synthesized POVs-$K_2Zn_2V_{10}O_{28}\cdot 16H_2O$ by the liquid-phase modulation method and dehydrated it into $K_2Zn_2V_{10}O_{28}$ (KZVO) material [38]. As shown in Fig. 5a, a prominent pair of redox peaks can be observed in CV tests, which indicate

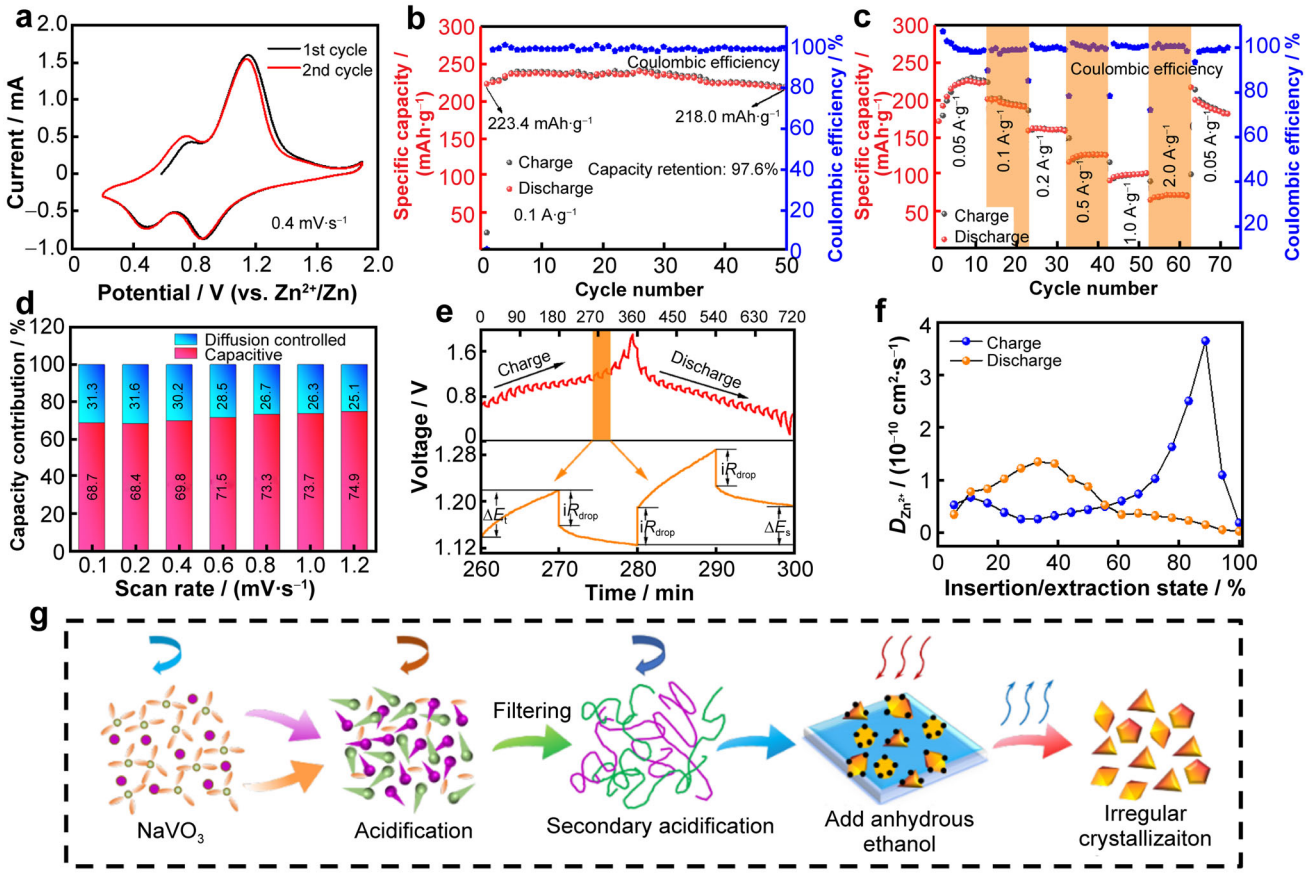

Fig. 5 **a** CV curves of KZVO cathode in the first and second cycles; **b** cycle capacity at 0.1 $A{\cdot}g^{-1}$; **c** rate performance of KZVO cathode; **d** percentage contribution of pseudo-capacitance at various scan rates; **e** GITT test curves at selected cycle (ΔE_t is value of voltage change during a charge/discharge step, iR_{drop} stands for voltage change when charge/discharge step and standing step are switched to each other, and ΔE_s is change of steady-state voltage during a single-step GITT experiment); **f** diffusion coefficients of Zn^{2+} in KZVO during cycle process. Reproduced with permission from Ref. [38]. Copyright 2022, Wiley–VCH GmbH. **g** Synthesis scheme of $Na_6V_{10}O_{28}{\cdot}18H_2O$. Reproduced with permission from Ref. [59]. Copyright 2022, Elsevier

the removal and insertion of Zn^{2+}. In addition, a slight difference existed between the oxidation peaks in the first two cycles, which was caused by the instability of the system due to the material activation during cycling [57]. Cycle performance and rate performance of KZVO/Zn-based cells were further carried out, and a capacity retention rate of 97.6% could be achieved with 50 cycles at 0.1 $A{\cdot}g^{-1}$ (Fig. 5b). Additionally, the average discharge specific capacities of KZVO were 225.7, 200.8, 161.2, 126.4, 100.8 and 71.1 $mAh{\cdot}g^{-1}$ at 0.05, 0.1, 0.2, 0.5, 1.0 and 2.0 $A{\cdot}g^{-1}$, respectively (Fig. 5c). Interestingly, a high reversible specific capacity of 216.8 $mAh{\cdot}g^{-1}$ was obtained as the current density was recovered to 0.05 $A{\cdot}g^{-1}$, confirming the fast Zn^{2+} storage behavior of KZVO. Capacitive behavior and diffusion behavior were analyzed in-depth by pseudo-capacitance calculations and galvanostatic intermittent titration technique (GITT) tests. By calculating the pseudo-capacitance contribution of KZVO at different scan rates, the percentage of capacitance contribution at the scan rates of 0.1, 0.2, 0.4, 0.6, 0.8, 1.0 and 1.2 $mV{\cdot}s^{-1}$ was found to be 68.7%, 68.4%, 69.8%, 71.5%, 73.3%, 73.7% and 74.9%, respectively (Fig. 5d). In general, the increase in capacitive contribution favors the storage of large amounts of Zn^{2+} on KZVO surface, thus leading to the rapid transfer of Zn^{2+} [58].

GITT test results indicated that the KZVO/Zn system exhibited a Zn^{2+} diffusion coefficient as high as 1×10^{-10} $cm^2{\cdot}s^{-1}$, which was several orders of magnitude higher than typical manganese oxides (Fig. 5e, f). High diffusion coefficients enable long cycling of KZVO materials even at high current densities, which may be facilitated by the high conductivity of the aqueous electrolyte and the KZVO crystal structure suitable for Zn^{2+} detachment. Apart from that, a series of ex-situ tests were performed to explore the zinc storage mechanism of the KZVO/Zn system. The results of ex-situ XRD, XPS and transmission electron microscopy (TEM) demonstrated that Zn^{2+} could be reversibly inserted and removed during the cycling process.

At the same time, the irreversible phase product $Zn_3(OH)_2V_2O_7{\cdot}2H_2O$ (defined as ZVOH) appeared during the cycling process, thus, the unique zinc storage behavior during the cycling process might originate from the combined effect of the irreversible phases ZVOH and KZVO. To further investigate the electrochemical behavior and zinc storage mechanism in this system, Cao et al. carried out a similar investigation based on the same series of POVs-$Na_6V_{10}O_{28}{\cdot}18H_2O$ [59]. $Na_6V_{10}O_{28}{\cdot}18H_2O$ was successfully prepared by pH adjustment and anhydrous ethanol precipitation (Fig. 5g), which is subjected to the subsequent electrochemical tests. GCD results revealed that $Na_6V_{10}O_{28}$ delivered outstanding rate performance and long cycle properties, with no significant capacity loss at 2 $A{\cdot}g^{-1}$ for 2000 cycles. Meanwhile, high capacitance contributions and high Zn^{2+} diffusion coefficients were similarly presented in the $Na_6V_{10}O_{28}$/Zn system, and the storage behavior of Zn^{2+} was further corroborated by ex-situ tests, which were consistent with the previous discussion. In short, those works offered novel opinions on the research and utilization of POVs in aqueous ZIBs and demonstrated that POVs materials are extremely promising electrode materials.

Other than the research that directly utilizes $(V_{10}O_{28})^{6-}$-based POVs as electrode materials, doping ions with POVs have also become a new research direction. Liu et al. doped decavanadate anions into polyaniline (PANI) by the electro-polymerization method and then employed them as cathode for aqueous ZIBs [60]. The precursors included Na_3VO_4, aniline and HCl. During the positive CV scan, the aniline was electro-polymerized to generate PANI and anions, e.g., $(V_{10}O_{28})^{6-}$ and Cl^-, and were doped into PANI polymer chain so as to achieve electrical neutrality. More specifically, Cl^- was doped into PANI by the negative scan, while $(V_{10}O_{28})^{6-}$ was trapped in PANI due to the steric hindrance. As indicated in the Raman spectrum (Fig. 6a), the symmetric stretching modes of the typical terminal V=O bonds belonging to $(V_{10}O_{28})^{6-}$ at 968 and 993 cm^{-1} were observed in PANI-$V_{10}O_{28}$. Similarly, symmetric and antisymmetric stretching vibrations of V–O–V ascribing to $(V_{10}O_{28})^{6-}$ were also presented in the FTIR spectrum [40]. These characteristic peaks suggested the successful doping of $(V_{10}O_{28})^{6-}$ into PANI. TEM images (Fig. 6b) revealed that PANI-$V_{10}O_{28}$ films were deposited on the exfoliated graphite/graphene sheets atop exfoliated graphite substrate (EG). These highly conductive graphite/graphene sheets were sandwiched in PANI film, facilitating electron transfer. High-angle-annular-dark-field scanning transmission electron microscopy (HAADF-STEM) images observed that many bright spots appeared (Fig. 6c), which represented the heaviest element vanadium in PANI-$V_{10}O_{28}$. The bright spots in STEM images primarily refer to $(V_{10}O_{28})^{6-}$ cluster in PANI-$V_{10}O_{28}$, which demonstrated $(V_{10}O_{28})^{6-}$ uniform doping in PANI chain. This distinctive structure allows full exposure of V-based active sites for charge storage, thereby improving the utilization of materials. To evaluate the electrochemical properties after doping, conventional Cl-doped PANI (defined as PANI-Cl) was applied as a control sample. As depicted in the EIS plots (Fig. 6d), PANI-$V_{10}O_{28}$ displayed a smaller equivalent series resistance (R_s) and charge transfer resistance (R_{ct}) than PANI-Cl, which suggests the better conductivity of PANI-$V_{10}O_{28}$. Consequently, PANI-$V_{10}O_{28}$ exhibited an enhanced rate performance compared with PANI-Cl (Fig. 6e). Moreover, PANI-$V_{10}O_{28}$ also showed much better cycle life, with only 18% capacity loss after 2000 cycles at 8 $A{\cdot}g^{-1}$ (Fig. 6f). To analyze the charge storage mechanism of PANI-$V_{10}O_{28}$ in 8 $mol{\cdot}L^{-1}$ $ZnCl_2$ solution, extensive ex-situ tests were performed. In general, during the electro-polymerization process, $(V_{10}O_{28})^{6-}$ will be incorporated into PANI and interact with the protonated N sites (–NH^+– and –NH^+=) to equilibrate the positive charges in the polymer chains (Fig. 6g). The decavanadate anions were trapped in the polymer as a result of the strong steric hindrance effect. Interestingly, the content of structural water also increased after cycling, which was explained by the insertion of $Zn(H_2O)_2Cl_4^{2-}$ during charging and the generation of $Zn_5(OH)_8Cl_2{\cdot}H_2O$ during discharging (Fig. 6h). This explanation was further corroborated by ex-situ SEM tests. The above results strongly supported the reversible proton-dependent redox reaction in the PANI-$V_{10}O_{28}$ electrode.

2.4 $(V_{10}O_{28})^{6-}$ in Li–S batteries

Li–S batteries are believed to be one of the most promising alternatives for high-energy battery applications, due to the very high capacity of both lithium and sulfur. However, the reduction of sulfur generates soluble polysulfide species (Li_2S_8, Li_2S_6 and Li_2S_4), which diffuse to the Li anode, get reduced, and then shuttle back to the cathode for further oxidization. This "oxidization/reduction" loop leads to the infamous polysulfide shuttling issue, which further results in the low capacity, poor cycling, and low Coulombic efficiency in Li–S batteries. Recently, considerable progress has been made regarding the utilization of anchoring materials to restrict the polysulfides (LiPSs) shuttling [61], but the interaction mechanism and restrain processes are still unclear. Therefore, investigating the interaction between these materials and LiPSs is of vital importance for Li–S batteries. This section highlights the interaction mechanism and electrochemical properties based on $(V_{10}O_{28})^{6-}$ in Li–S batteries.

Li et al. firstly introduced $(NH_4)_6V_{10}O_{28}$ (denoted as NVO) clusters as sulfur fixation materials [62]. They found

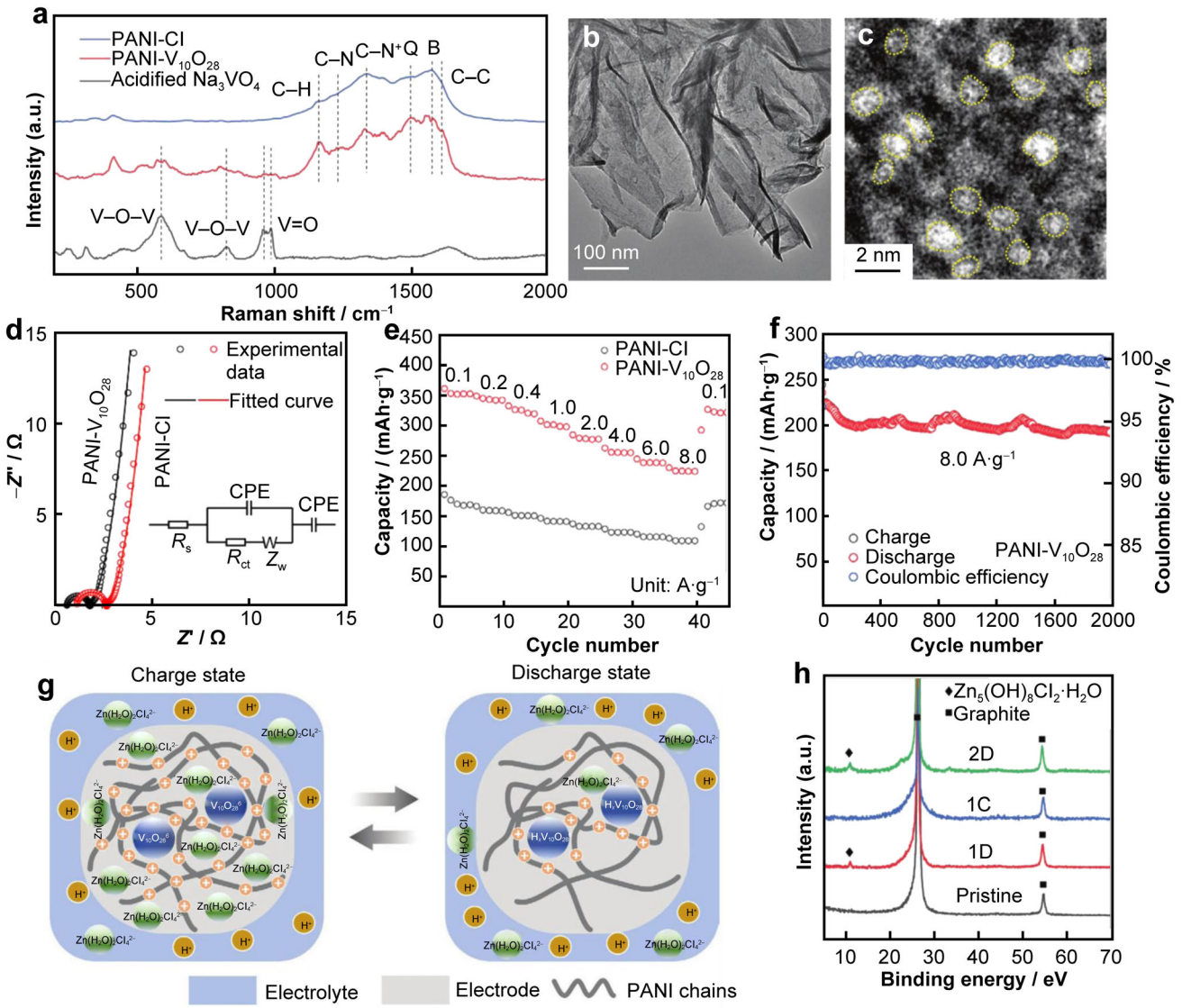

Fig. 6 **a** Comparison of Raman spectra among PANI-Cl, PANI-$V_{10}O_{28}$ and acidified Na_3VO_4; **b** TEM images and **c** HAADF-STEM images of PANI-$V_{10}O_{28}$; **d** EIS plots and **e** rate performance between PANI-$V_{10}O_{28}$ and PANI-Cl (impedance is expressed by Z, real part Z' is called resistance and imaginary part Z'' is called reactance); **f** long-cycle performance of PANI-$V_{10}O_{28}$; **g** schematic illustration of PANI-$V_{10}O_{28}$'s energy storage mechanism; **h** XRD patterns of PANI-$V_{10}O_{28}$ in various charge states. Reproduced with permission from Ref. [60]. Copyright 2022, Wiley–VCH GmbH

that these clusters exhibited excellent electrochemical properties and led to a distinctive two-step progressive sulfur fixation mechanism. Based on the complex structure of NVO, exploration and principal research were carried out for the absorption process in the reaction. Density-functional theory (DFT) calculation manifested that the interaction energy between Li_2S_n species and NVO was 1.6 times higher than Li–O interaction alone, which is owing to the double interaction of Li–O and V–S. Therefore, by this strong interaction, the application of NVO to Li–S batteries extended the lifetime of Li–S batteries. To further observe the interactions between NVO and LiPSs, a series of tests were performed including ultraviolet–visible absorption spectra, XPS analysis, ultra-fast transient absorption (TA) spectra, and XRD tests. The above tests lead to the following conclusions: i) NVO presented a strong adsorption ability to LiPSs. ii) Chemical interactions trapped LiPSs inside the cathode and thus improving the cycling stability of the cell. iii) Electron transfer processes existed between LiPSs and NVO. iv) Changes in the crystal configuration of NVO were driven by small changes in the positions of V and O during the interactions. Likewise, the strong adsorption between LiPSs and NVO was further verified by visualizing the electrochemical experiments as depicted in Fig. 7a. Interestingly, the electrolyte color of conventional electrodes (CE) + NVO (the electrodes containing 10 wt%

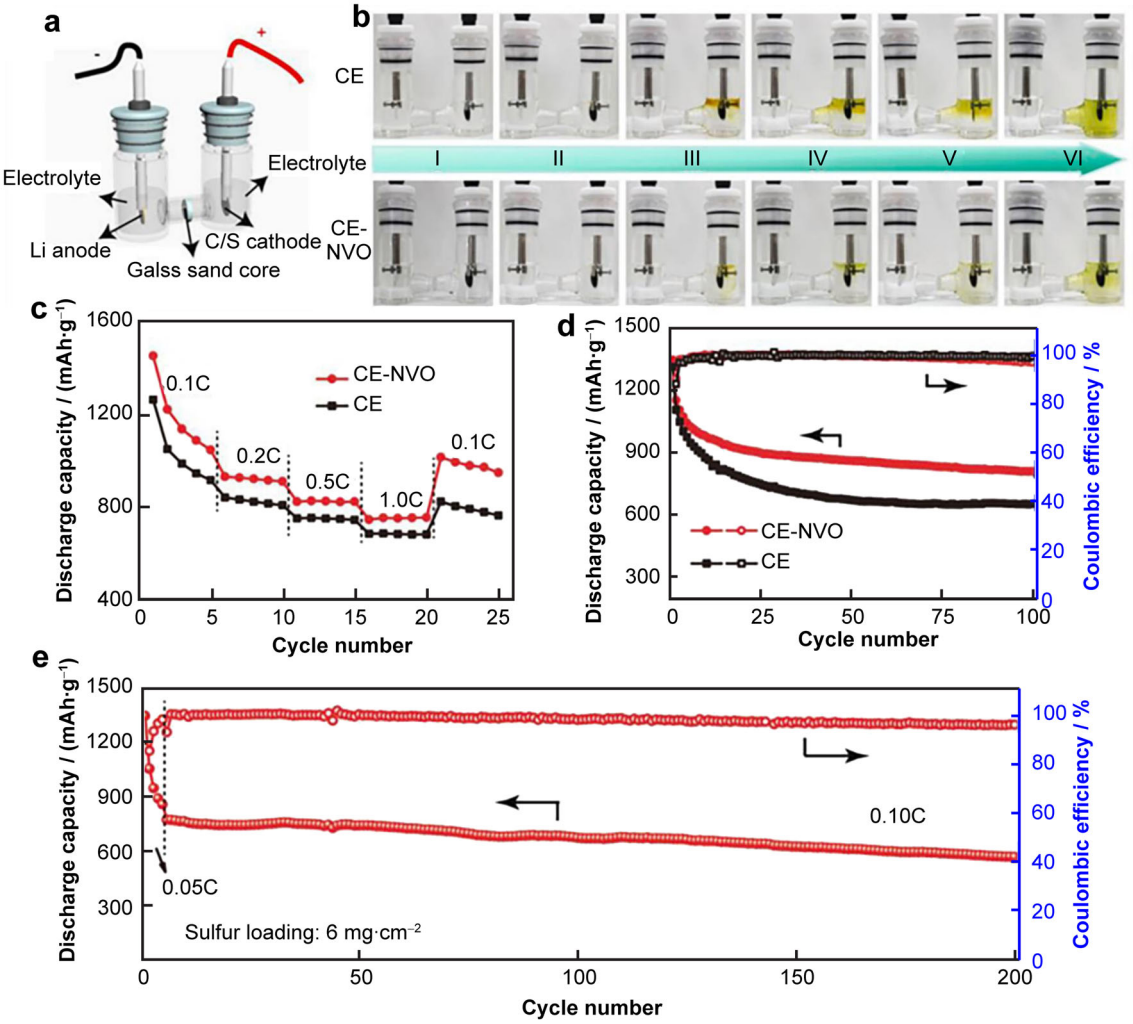

Fig. 7 **a** Illustration of experimental visualization device; **b** color change of electrolyte in two devices at different discharge states; **c** rate capability and **d** cycle stability of CE-NVO and pure CE cathodes; **e** cycling stability of high-sulfur-loaded CE-NVO as cathode for Li–S batteries. Reproduced with permission from Ref. [62]. Copyright 2020, Elsevier

NVO) batteries was significantly lighter than that of CE batteries at different discharge states (Fig. 7b), which confirmed that NVO could successfully restrict LiPSs and avoid their diffusion from the cathode into the electrolyte. Both rate performance (Fig. 7c) and cycling performance (Fig. 7d) tests illustrate the superior performance of electrodes with NVO present. In addition to the conventional tests, achieving a high area loading cathode for practical Li–S battery applications is also crucial. The cycling capacity of a high sulfur-loading CE-NVO cathode (sulfur-loading of 6 $mg{\cdot}cm^{-2}$) was tested at 0.1C and showed that the cell could achieve a high reversible capacity of 781 $mAh{\cdot}g^{-1}$. Moreover, after activation at a current density of 0.05C, the decay rate of each cycle was about 0.1% during 200 cycles (Fig. 7e). In conclusion, the explicit interaction process and ultra-strong double interaction force in the whole reaction allow such excellent performance and also pave the way for broadening the application of sulfur-fixing materials.

3 Scientific challenges and strategies

Although substantial progress has been achieved in the investigation of $(V_{10}O_{28})^{6-}$-cluster derivatives as battery electrode materials, extensive problems remain to be solved. The corresponding scientific strategies are proposed in this section as follows (Fig. 8).

(1) Improving poor electrochemical properties. As revealed in Table 1, those $(V_{10}O_{28})^{6-}$-based electrode materials mentioned above do not exhibit particularly outstanding electrochemical performance compared with other materials (e.g., vanadium oxides [63, 64] and metal organic frameworks (MOFs)-based

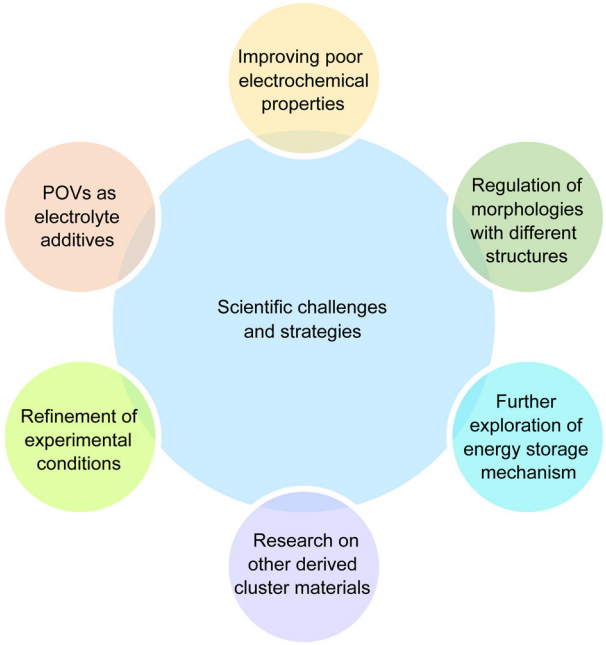

Fig. 8 Scientific challenges and strategies of $(V_{10}O_{28})^{6-}$-based electrode materials

materials [65, 66]). Therefore, it is urgent to find approaches to improve their electrochemical properties effectively. Many relevant modification methods have been employed for electrode materials, including nanostructure regulating [67], pre-intercalation of guest species [68, 69], introduction of electrolyte additives [7, 70], surface coating [71], and introduction of defects [72–74]. By these modification methods, the insertion and removal of the ions during the reaction can be dramatically improved.

(2) Regulation of morphologies with different structures. Typically, various morphologies are linked to counter cation directed crystallization processes [46, 75]. Morphologies of the material often play a crucial role in the process of electrochemical reactions, and different morphologies will produce distinct energy storage behaviors. On the basis of the current research, we find that most of the morphologies discussed are nano-rods/wires/tubes/sheets/flowers/particles [76]. Since the existing $(V_{10}O_{28})^{6-}$-based materials tend to display relatively common morphologies, preparing cluster materials with sophisticated morphologies by directional modulation is a fascinating strategy, which may also improve the electrochemical properties of the system to some degree.

(3) Further exploration of the energy storage mechanism. At present, the energy storage mechanism about $(V_{10}O_{28})^{6-}$-based electrode materials in different battery systems mainly involves the intercalation process of Li^+ in LIBs accompanied by the change of the chemical valence of vanadium, the predominant insertion of Na^+ in SIBs between the interstices of $(V_{10}O_{28})^{6-}$ clusters rather than the crystal structure, the reversible (de)insertion of Zn^{2+} and the irreversible production of alkali vanadate in ZIBs, the two-step progressive sulfur fixation mechanism in Li–S batteries, etc. [38, 43, 49, 59, 62]. Nevertheless, there is still a paucity of mechanistic research on different systems and materials with various $(V_{10}O_{28})^{6-}$ cluster derivatives, so in-depth investigation of the energy storage mechanism in such materials is also essential for the subsequent work.

(4) Research on other derived cluster materials. POVs display significant advantages in the energy storage field thanks to their superior redox properties. Except the most investigated decavanadate anion, there exist a variety of other cluster structures, including $[V_3O_9]^{3-}$, $[V_4O_{12}]^{4-}$, $[V^{IV}{}_8V^{V}{}_7O_{36}]^{5-}$, $[V^{IV}{}_{11}V^{V}{}_5O_{38}]^{7-}$, $[V_{15}O_{42}]^{9-}$, $[V^{IV}{}_{16}V^{V}{}_{18}O_{82}]^{10-}$, etc. [36]. With the different spatial structures of cluster materials, their electrochemical reaction processes appear to be more diversified, so it would be an excellent idea if the subsequent work could be developed toward the derivatives corresponding to such substances. Besides that, novel designs of these cluster materials are also feasible, such as the design of amorphous zinc storage materials via Ag^+ [77].

(5) Refinement of experimental conditions. Besides the above-mentioned cases, a deeper study of the influencing factors related to experimental conditions (e.g., electrolyte composition [7, 78], reaction pH [79], temperature [80], etc.) is essential, as well as the effect of changes in the substitution of metal atoms in the cluster lattice on the material properties. Just as the introduction of NO_3^- could change the solvation structure of Li^+ and thus facilitate the effective desolvation of Li^+ to improve the battery performance [81], aqueous polyacid clusters may also be available as electrolyte additives to boost the interfacial stability in the reaction and consequently enhance the stability of aqueous batteries.

(6) POVs as electrolyte additives. Currently, the development of reliable electrolytes has become an emerging research hotspot in the field, especially the employment of various organic or inorganic compounds as electrolyte additives [82]. Other than the typical addition of Mn^{2+}, Na^+, etc., to the electrolyte to inhibit material dissolution and phase change, searching for new electrolyte additives is also critical [7, 83]. Among them, aqueous POVs clusters with high proton conductivity and favorable chemical stability are promising electrolytes.

Unfortunately, there is still a lack of research on POVs clusters as electrolyte additives. Therefore, subsequent research could expand to the construction of functionalized electrolyte additives based on POVs, which may help solve the Zn metal corrosion and hydrogen evolution problem in aqueous battery systems.

4 Conclusion

Based on the above introduction and discussion, $(V_{10}O_{28})^{6-}$-based compounds hold great promise as advanced electrode materials for rechargeable batteries, due to their stable structure, easy preparation, and strong coordination ability. However, the implementation of $(V_{10}O_{28})^{6-}$-based electrode materials in the battery field still faces some intrinsic challenges. From the above discussion, poor cycling and rate performance, irregular morphology, and unclear energy storage mechanism are fundamental problems that need to be urgently addressed for this type of materials. Accordingly, regulating nanostructures, refining synthesis methods, optimizing electrolytes, and new testing methods are effective approaches to tackle the above problems. With efforts, the electrochemical properties of such materials are expected to be further enhanced, which will also be a competitive electrode material in next-generation rechargeable batteries. In conclusion, this review puts forward a comprehensive review of the research progress of $(V_{10}O_{28})^{6-}$-based electrode materials, which will provide helpful references for future research.

Acknowledgements This work was financially supported by the National Natural Science Foundation of China (Nos. 52071132, U21A20284 and U1904216), Zhongyuan Thousand People Plan-The Zhongyuan Youth Talent Support Program (in Science and Technology), China (No. ZYQR201810139), the Innovative Funds Plan of Henan University of Technology, China (No. 2020ZKCJ04), and the Natural Science Foundation of Henan, China (No. 222300420138). Additionally, Dr. Xianyong Wu acknowledges the support from the NSF Center for the Advancement of Wearable Technologies (No. 1849243).

Declarations

Conflict of interests The authors declare that they have no conflict of interest.

References

[1] Zampardi G, Mantia FL. Prussian blue analogues as aqueous Zn-ion batteries electrodes: Current challenges and future perspectives. Curr Opin Electrochem. 2020;21:84. https://doi.org/10.1016/j.coelec.2020.01.014.

[2] Zhu LM, Wang ZH, Wang L, Xie LL, Li JJ, Cao XY. ZnSe embedded in N-doped carbon nanocubes as anode materials for high-performance Li-ion batteries. Chem Eng J. 2019;364:503. https://doi.org/10.1016/j.cej.2019.01.191.

[3] Wei FL, Zhang QP, Zhang P, Tian WQ, Dai KH, Zhang L, Mao J, Shao GS. Review-Research progress on layered transition metal oxide cathode materials for sodium ion batteries. J Electrochem Soc. 2021;168(5):050524. https://doi.org/10.1149/1945-7111/abf9bf.

[4] Yi TF, Qiu LY, Qu JP, Liu HY, Zhang JH, Zhu YR. Towards high-performance cathodes: design and energy storage mechanism of vanadium oxides-based materials for aqueous Zn-ion batteries. Coord Chem Rev. 2021;446:214124. https://doi.org/10.1016/j.ccr.2021.214124.

[5] Dong Y, Miao LC, Ma GQ, Di SL, Wang YY, Wang LB, Xu JZ, Zhang N. Non-concentrated aqueous electrolytes with organic solvent additives for stable zinc batteries. Chem Sci. 2021;12(16):5843. https://doi.org/10.1039/d0sc06734b.

[6] Xu J, Peng Y, Xing WQ, Ding ZY, Zhang ST, Pang H. Metal-organic frameworks marry carbon: booster for electrochemical energy storage. J Energy Storage. 2022;53:105104. https://doi.org/10.1016/j.est.2022.105104.

[7] Wan F, Zhang LL, Dai X, Wang XY, Niu ZQ, Chen J. Aqueous rechargeable zinc/sodium vanadate batteries with enhanced performance from simultaneous insertion of dual carriers. Nat Commun. 2018;9(1):1656. https://doi.org/10.1038/s41467-018-04060-8.

[8] Ni LS, Guo RT, Fang SS, Chen J, Gao JQ, Mei Y, Zhang S, Deng WT, Zou GQ, Hou HS, Ji XB. Crack-free single-crystalline Co-free Ni-rich $LiNi_{0.95}Mn_{0.05}O_2$ layered cathode. eScience. 2022;2(1):116. https://doi.org/10.1016/j.esci.2022.02.006.

[9] Wang B, Ruan TT, Chen Y, Jin F, Peng L, Zhou Y, Wang DL, Dou SX. Graphene-based composites for electrochemical energy storage. Energy Storage Mater. 2020;24:22. https://doi.org/10.1016/j.ensm.2019.08.004.

[10] Wei TT, Peng PP, Ji YR, Zhu YR, Yi TF, Xie Y. Rational construction and decoration of $Li_5Cr_7Ti_6O_{25}$@C nanofibers as stable lithium storage materials. J Energy Chem. 2022;71:400. https://doi.org/10.1016/j.jechem.2022.04.017.

[11] Liu YY, Lv TT, Wang H, Guo XT, Liu CS, Pang H. Nsutite-type VO_2 microcrystals as highly durable cathode materials for aqueous zinc-ion batteries. Chem Eng J. 2021;417:128408. https://doi.org/10.1016/j.cej.2021.128408.

[12] Zhu S, Sheng J, Ni JF, Li Y. 3D vertical arrays of nanomaterials for microscaled energy storage devices. Accounts Mater Res. 2021;2(12):1215. https://doi.org/10.1021/accountsmr.1c00175.

[13] Wang ZQ, Zhou M, Qin LP, Chen MH, Chen ZX, Guo S, Wang LB, Fang GZ, Liang SQ. Simultaneous regulation of cations and anions in an electrolyte for high-capacity, high-stability aqueous zinc–vanadium batteries. eScience. 2022;2(2):209. https://doi.org/10.1016/j.esci.2022.03.002.

[14] Ding GC, Zhu LM, Yang Q, Xie LL, Cao XY, Wang YL, Liu JP, Yang XL. NaV_3O_8/poly(3,4-ethylenedioxythiophene) composites as high-rate and long-lifespan cathode materials for reversible sodium storage. Rare Met. 2020;39(8):865. https://doi.org/10.1007/s12598-020-01452-y.

[15] Zhou T, Han Q, Xie LL, Yang XL, Zhu LM, Cao XY. Recent developments and challenges of vanadium oxides (V_xO_y) cathodes for aqueous zinc-ion batteries. Chem Rec. 2022;22(4):e202100275. https://doi.org/10.1002/tcr.202100275.

[16] Wang F, Liu Y, Wei HJ, Li TF, Xiong XH, Wei SZ, Ren FZ, Volinsky AA. Recent advances and perspective in metal coordination materials-based electrode materials for potassium-ion batteries. Rare Met. 2021;40(2):448. https://doi.org/10.1007/s12598-020-01649-1.

[17] Geng PB, Wang L, Du M, Bai Y, Li WT, Liu YF, Chen SQ, Braunstein P, Xu Q, Pang H. MIL-96-Al for Li-S batteries: shape or size? Adv Mater. 2022;34(4):2107836. https://doi.org/10.1002/adma.202107836.

[18] Ma LB, Zhang WJ, Wang L, Hu Y, Zhu GY, Wang YR, Chen RP, Chen T, Tie ZX, Liu J, Jin Z. Strong capillarity, chemisorption, and electrocatalytic capability of crisscrossed nanostraws enabled flexible, high-rate, and long-cycling lithium-sulfur batteries. ACS Nano. 2018;12(5):4868. https://doi.org/10.1021/acsnano.8b01763.

[19] Zhu LM, Ding GC, Han Q, Miao YX, Li X, Yang XL, Chen L, Wang GK, Xie LL, Cao XY. Enhancing electrochemical performances of small quinone toward lithium and sodium energy storage. Rare Met. 2022;41(2):425. https://doi.org/10.1007/s12598-021-01813-1.

[20] Jiang Y, Wang YC, Ni JF, Li L. Molybdenum-based materials for sodium-ion batteries InfoMat. 2021;3(4):339. https://doi.org/10.1002/inf2.12175.

[21] Ni JF, Li L. Cathode architectures for rechargeable ion batteries: progress and perspectives. Adv Mater. 2020;32(28):e2000288. https://doi.org/10.1002/adma.202000288.

[22] Feng J, Luo SH, Cai KX, Yan SX, Wang Q, Zhang YH, Liu X. Research progress of tunnel-type sodium manganese oxide cathodes for SIBs. Chin Chem Lett. 2022;33(5):2316. https://doi.org/10.1016/j.cclet.2021.09.077.

[23] Xiao J, Li X, Tang KK, Wang DD, Long MQ, Gao H, Chen WH, Liu CT, Liu H, Wang GX. Recent progress of emerging cathode materials for sodium ion batteries. Mat Chem Front. 2021;5(10):3735. https://doi.org/10.1039/d1qm00179e.

[24] Yan WW, Yang SY, Huang YY, Yang Y, Yuan GH. A review on doping/coating of nickel-rich cathode materials for lithium-ion batteries. J Alloys Compd. 2020;819:153048. https://doi.org/10.1016/j.jallcom.2019.153048.

[25] Pang GY, Zhuang WD, Bai XT, Ban LQ, Zhao CR, Sun XY. Research advances of Co-free and Ni-rich $LiNi_xMn_{1-x}O_2$ ($0.5<x<1$) cathode materials. Chin J Rare Met. 2020;44(9):996. https://doi.org/10.13373/j.cnki.cjrm.xy19030056.

[26] Yu X, Hu F, Guo ZQ, Liu L, Song GH, Zhu K. High-performance $Cu_{0.95}V_2O_5$ nanoflowers as cathode materials for aqueous zinc-ion batteries. Rare Met. 2022;41(1):29. https://doi.org/10.1007/s12598-021-01771-8.

[27] Anjass M, Lowe GA, Streb C. Molecular vanadium oxides for energy conversion and energy storage: current trends and emerging opportunities. Angew Chem Int Ed. 2021;60(14):7522. https://doi.org/10.1002/anie.202010577.

[28] Xue YT, Chen Y, Shen XP, Zhong A, Ji ZY, Cheng J, Kong LR, Yuan AH. Decoration of nickel hexacyanoferrate nanocubes onto reduced graphene oxide sheets as high-performance cathode material for rechargeable aqueous zinc-ion batteries. J Colloid Interface Sci. 2021;609:297. https://doi.org/10.1016/j.jcis.2021.12.014.

[29] Wang JJ, Wang JX, Jiang YL, Xiong FY, Tan SS, Qiao F, Chen JH, An QY, Mai LQ. $CaV_6O_{16}{\cdot}2.8H_2O$ with Ca^{2+} pillar and water lubrication as a high-rate and long-life cathode material for Ca-ion batteries. Adv Funct Mater. 2022;32(25):2113030. https://doi.org/10.1002/adfm.202113030.

[30] Luo XY, Peng WC, Li Y, Zhang FB, Fan XB. Understanding of the electrochemical behaviors of aqueous zinc-manganese batteries: reaction processes and failure mechanisms. Green Energy Environ. 2022;7:858. https://doi.org/10.1016/j.gee.2021.08.006.

[31] Du M, Miao ZY, Li HZ, Zhang F, Sang YH, Wei L, Liu H, Wang SH. Oxygen-vacancy and phosphate coordination triggered strain engineering of vanadium oxide for high-performance aqueous zinc ion storage. Nano Energy. 2021;89:106477. https://doi.org/10.1016/j.nanoen.2021.106477.

[32] Wu XW, Xiang YH, Peng QJ, Wu XS, Li YH, Tang F, Song RC, Liu ZX, He ZQ, Wu XM. Green-low-cost rechargeable aqueous zinc-ion batteries using hollow porous spinel $ZnMn_2O_4$ as the cathode material. J Mater Chem A. 2017;5(34):17990. https://doi.org/10.1039/c7ta00100b.

[33] Wang YB, Yang Q, Guo X, Yang S, Chen A, Liang GJ, Zhi CY. Strategies of binder design for high-performance lithium-ion batteries: a mini review. Rare Met. 2022;41(3):745. https://doi.org/10.1007/s12598-021-01816-y.

[34] Li QY, Zhang L, Dai JL, Tang H, Li Q, Xue HG, Pang H. Polyoxometalate-based materials for advanced electrochemical energy conversion and storage. Chem Eng J. 2018;351:441. https://doi.org/10.1016/j.cej.2018.06.074.

[35] Ji YC, Hu J, Huang LJ, Chen W, Streb C, Song YF. Covalent attachment of Anderson-type polyoxometalates to single-walled carbon nanotubes gives enhanced performance electrodes for lithium ion batteries. Chemistry. 2015;21(17):6469. https://doi.org/10.1002/chem.201500218.

[36] Monakhov KY, Bensch W, Kogerler P. Semimetal-functionalised polyoxovanadates. Chem Soc Rev. 2015;44(23):8443. https://doi.org/10.1039/c5cs00531k.

[37] Yang K, Hu YY, Li LY, Cui LL, He L, Wang SJ, Zhao JW, Song YF. First high-nuclearity mixed-valence polyoxometalate with hierarchical interconnected Zn^{2+} migration channels as an advanced cathode material in aqueous zinc-ion battery. Nano Energy. 2020;74:104851. https://doi.org/10.1016/j.nanoen.2020.104851.

[38] Zhou T, Zhu LM, Xie LL, Han Q, Yang XL, Cao XY, Ma JM. New insight on $K_2Zn_2V_{10}O_{28}$ as an advanced cathode for rechargeable aqueous zinc-ion batteries. Small. 2022;18(12):2107102. https://doi.org/10.1002/smll.202107102.

[39] Xing ZY, Xu GF, Xie XS, Chen MJ, Lu BA, Zhou J, Liang SQ. Highly reversible zinc-ion battery enabled by suppressing vanadium dissolution through inorganic Zn^{2+} conductor electrolyte. Nano Energy. 2021;90:106621. https://doi.org/10.1016/j.nanoen.2021.106621.

[40] Sanchez-Lara E, Trevino S, Sanchez-Gaytan BL, Sanchez-Mora E, Eugenia Castro M, Melendez-Bustamante FJ, Mendez-Rojas MA, Gonzalez-Vergara E. Decavanadate salts of cytosine and metformin: A combined experimental-theoretical study of potential metallodrugs against diabetes and cancer. Front Chem. 2018;6:402. https://doi.org/10.3389/fchem.2018.00402.

[41] Aureliano M, Gumerova NI, Sciortino G, Garribba E, McLauchlan CC, Rompel A, Crans DC. Polyoxidovanadates' interactions with proteins: An overview. Coord Chem Rev. 2022;454:214344. https://doi.org/10.1016/j.ccr.2021.214344.

[42] Ueda T. Electrochemistry of polyoxometalates: from fundamental aspects to applications. ChemElectroChem. 2018;5(6):823. https://doi.org/10.1002/celc.201701170.

[43] Xie AL, Ma CA, Wang LB, Chu YQ. $Li_6V_{10}O_{28}$, a novel cathode material for Li-ion battery. Electrochim Acta. 2007;52(9):2945. https://doi.org/10.1016/j.electacta.2006.08.069.

[44] Liu HW, Wang J. The synthesis, structure, and electrochemical properties of a novel rods-shaped $Li_6V_{10}O_{28}$ for lithium-ion batteries. Ionics. 2009;16(4):379. https://doi.org/10.1007/s11581-009-0414-5.

[45] Chen HY, Friedl J, Pan CJ, Haider A, Al-Oweini R, Cheah YL, Lin MH, Kortz U, Hwang BJ, Srinivasan M, Stimming U. In situ X-ray absorption near edge structure studies and charge transfer kinetics of $Na_6[V_{10}O_{28}]$ electrodes. Phys Chem Chem Phys. 2017;19(4):3358. https://doi.org/10.1039/c6cp05768c.

[46] Lu SS, Lv Y, Ma WQ, Lei XF, Zhang RE, Liu H, Liu XZ. Boosting the ultrastable Li storage performance in electron-sponge-like polyoxovanadates by constructing inorganic 3D structures. Inorg Chem Front. 2017;4(12):2012. https://doi.org/10.1039/c7qi00581d.

[47] Jiang CH, Tang ZL, Wang ST, Zhang ZT. A truncated octahedral spinel $LiMn_2O_4$ as high-performance cathode material for ultrafast and long-life lithium-ion batteries. J Power Sources. 2017;357:144. https://doi.org/10.1016/j.jpowsour.2017.04.079.
[48] Zhang T, Yue HJ, Qiu HL, Wei YJ, Wang CZ, Chen G, Zhang D. Nano-particle assembled porous core-shell $ZnMn_2O_4$ microspheres with superb performance for lithium batteries. Nanotechnology. 2017;28(10):105403. https://doi.org/10.1088/1361-6528/aa5a49.
[49] Hartung S, Bucher N, Chen HY, Al-Oweini R, Sreejith S, Borah P, Zhao YL, Kortz U, Stimming U, Hoster HE, Srinivasan M. Vanadium-based polyoxometalate as new material for sodium-ion battery anodes. J Power Sources. 2015;288:270. https://doi.org/10.1016/j.jpowsour.2015.04.009.
[50] Frost RL, Erickson KL, Weier ML, Carmody O. Raman and infrared spectroscopy of selected vanadates. Spectroc Acta Pt A-Molec Biomolec Spectr. 2005;61(5):829. https://doi.org/10.1016/j.saa.2004.06.006.
[51] Ponrouch A, Dedryvère R, Monti D, Demet AE, Ateba Mba JM, Croguennec L, Masquelier C, Johansson P, Palacín MR. Towards high energy density sodium ion batteries through electrolyte optimization. Energy Environ Sci. 2013;6(8):2361. https://doi.org/10.1039/c3ee41379a.
[52] Ponrouch A, Goñi AR, Palacín MR. High capacity hard carbon anodes for sodium ion batteries in additive free electrolyte. Electrochem Commun. 2013;27:85. https://doi.org/10.1016/j.elecom.2012.10.038.
[53] Li XR, Cheng HY, Hu H, Pan KM, Yuan TT, Xia WT. Recent advances of vanadium-based cathode materials for zinc-ion batteries. Chin Chem Lett. 2021;32(12):3753. https://doi.org/10.1016/j.cclet.2021.04.045.
[54] Zhou T, Xiao HR, Xie LL, Han Q, Qiu XJ, Xiao YM, Yang XL, Zhu LM, Cao XY. Research on the electrochemical performance of polyoxovanadate material $K_4Na_2V_{10}O_{28}$ as a novel aqueous zinc-ion batteries cathode. Electrochim Acta. 2022;424:140621. https://doi.org/10.1016/j.electacta.2022.140621.
[55] Ruan PC, Liang SQ, Lu BA, Fan HJ, Zhou J. Design strategies for high-energy-density aqueous zinc batteries. Angew Chem Int Ed. 2022;61(17):e202200598. https://doi.org/10.1002/anie.202200598.
[56] Cai YS, Liu F, Luo ZG, Fang GZ, Zhou J, Pan AQ, Liang SQ. Pilotaxitic $Na_{1.1}V_3O_{7.9}$ nanoribbons/graphene as high-performance sodium ion battery and aqueous zinc ion battery cathode. Energy Storage Mater. 2018;13:168. https://doi.org/10.1016/j.ensm.2018.01.009.
[57] Dai X, Wan F, Zhang LL, Cao HM, Niu ZQ. Freestanding graphene/VO_2 composite films for highly stable aqueous Zn-ion batteries with superior rate performance. Energy Storage Mater. 2019;17:143. https://doi.org/10.1016/j.ensm.2018.07.022.
[58] Wu SG, Liu S, Hu LH, Chen SH. Constructing electron pathways by graphene oxide for V_2O_5 nanoparticles in ultra-high-performance and fast charging aqueous zinc ion batteries. J Alloys Compd. 2021;878:160324. https://doi.org/10.1016/j.jallcom.2021.160324.
[59] Zhou T, Xie LL, Han Q, Yang XL, Zhu LM, Cao XY. Investigation of $Na_6V_{10}O_{28}$ as a promising rechargeable aqueous zinc-ion batteries cathode. Chem Eng J. 2022;445:136789. https://doi.org/10.1016/j.cej.2022.136789.
[60] Zhang MY, Song Y, Mu XJ, Yang D, Qin ZM, Guo D, Sun XQ, Liu XX. Decavanadate doped polyaniline for aqueous zinc batteries. Small. 2022;18(16):2107689. https://doi.org/10.1002/smll.202107689.
[61] Wang ML, Yin D, Cao YD, Dong XY, Gao GG, Hu X, Jin C, Fan LL, Yu J, Liu H. Surface modification of hollow capsule by Dawson-type polyoxometalate as sulfur hosts for ultralong-life lithium-sulfur batteries. Chin Chem Lett. 2022;33(9):4350. https://doi.org/10.1016/j.cclet.2021.11.043.
[62] Yu Y, Li TY, Zhang HZ, Luo Y, Zhang HM, Zhang JW, Yan JW, Li XF. Principle of progressively and strongly immobilizing polysulfides on polyoxovanadate clusters for excellent Li-S batteries application. Nano Energy. 2020;71:104596. https://doi.org/10.1016/j.nanoen.2020.104596.
[63] Chen LL, Yang ZH, Huang YG. Monoclinic VO_2(D) hollow nanospheres with super-long cycle life for aqueous zinc ion batteries. Nanoscale. 2019;11(27):13032. https://doi.org/10.1039/c9nr03129d.
[64] Wan F, Huang S, Cao HM, Niu ZQ. Freestanding potassium vanadate/carbon nanotube films for ultralong-life aqueous zinc-ion batteries. ACS Nano. 2020;14(6):6752. https://doi.org/10.1021/acsnano.9b10214.
[65] Wang L, Wang ZH, Xie LL, Zhu LM, Cao XY. ZIF-67-derived N-doped Co/C nanocubes as high-performance anode materials for lithium-ion batteries. ACS Appl Mater Interfaces. 2019;11(18):16619. https://doi.org/10.1021/acsami.9b03365.
[66] Yang P, Zhao WL, Shkurenko A, Belmabkhout Y, Eddaoudi M, Dong XC, Alshareef HN, Khashab NM. Polyoxometalate-cyclodextrin metal-organic frameworks: from tunable structure to customized storage functionality. J Am Chem Soc. 2019;141(5):1847. https://doi.org/10.1021/jacs.8b11998.
[67] Fang YJ, Yu XY, Lou XW. Nanostructured electrode materials for advanced sodium-ion batteries. Matter. 2019;1(1):90. https://doi.org/10.1016/j.matt.2019.05.007.
[68] Yang YQ, Tang Y, Fang GZ, Shan LT, Guo JS, Zhang WY, Wang C, Wang LB, Zhou J, Liang SQ. Li^+ intercalated $V_2O_5{\cdot}nH_2O$ with enlarged layer spacing and fast ion diffusion as an aqueous zinc-ion battery cathode. Energy Environ Sci. 2018;11(11):3157. https://doi.org/10.1039/c8ee01651h.
[69] Zhang DD, Cao J, Yue YL, Pakornchote T, Bovornratanaraks T, Han JT, Zhang XY, Qin JQ, Huang YH. Two birds with one stone: boosting zinc-ion insertion/extraction kinetics and suppressing vanadium dissolution of V_2O_5 via La^{3+} incorporation enable advanced zinc-ion batteries. ACS Appl Mater Interfaces. 2021;13(32):38416. https://doi.org/10.1021/acsami.1c11531.
[70] Lu C, Chen X. All-temperature flexible supercapacitors enabled by antifreezing and thermally stable hydrogel electrolyte. Nano Lett. 2020;20(3):1907. https://doi.org/10.1021/acs.nanolett.9b05148.
[71] Zhao DX, Mo LL, Han Q, Xie LL, Zhu LM, Cao XY. Nitrogen-doped carbon-coated $Li_3V_2(PO_4)_3$ as cathode materials for high-performance lithium storage. Ionics. 2021;27(2):507. https://doi.org/10.1007/s11581-020-03878-x.
[72] Yu PF, Zhou JX, Zheng MT, Li MR, Hu H, Xiao Y, Liu YL, Liang YR. Boosting zinc ion energy storage capability of inert MnO cathode by defect engineering. J Colloid Interface Sci. 2021;594:540. https://doi.org/10.1016/j.jcis.2021.03.071.
[73] Zhang N, Jia M, Dong Y, Wang YY, Xu JZ, Liu YC, Jiao LF, Cheng FY. Hydrated layered vanadium oxide as a highly reversible cathode for rechargeable aqueous zinc batteries. Adv Funct Mater. 2019;29(10):1807331. https://doi.org/10.1002/adfm.201807331.
[74] Gao Y, Yin JY, Xu X, Cheng YH. Pseudocapacitive storage in cathode materials of aqueous zinc ion batteries toward high power and energy density. J Mater Chem A. 2022;10(18):9773. https://doi.org/10.1039/d2ta01014c.
[75] Zhu QN, Wang ZY, Wang JW, Liu XY, Yang D, Cheng LW, Tang MY, Qin Y, Wang H. Challenges and strategies for ultrafast aqueous zinc-ion batteries. Rare Met. 2021;40(2):309. https://doi.org/10.1007/s12598-020-01588-x.
[76] Zhou T, Zhu LM, Xie LL, Han Q, Yang XL, Chen L, Wang GK, Cao XY. Cathode materials for aqueous zinc-ion batteries: a

mini review. J Colloid Interface Sci. 2021;605:828. https://doi.org/10.1016/j.jcis.2021.07.138.
[77] Yang K, Ying YX, Cui LL, Sun JC, Luo H, Hu YY, Zhao JW. Stable aqueous Zn-Ag and Zn-polyoxometalate hybrid battery driven by successive Ag^{+} cation and polyoxoanion redox reactions. Energy Storage Mater. 2021;34:203. https://doi.org/10.1016/j.ensm.2020.09.011.
[78] Zhang TS, Tang Y, Guo S, Cao XX, Pan AQ, Fang GZ, Zhou J, Liang SQ. Fundamentals and perspectives in developing zinc-ion battery electrolytes: A comprehensive review. Energy Environ Sci. 2020;13(12):4625. https://doi.org/10.1039/d0ee02620d.
[79] Fitz O, Bischoff C, Bauer M, Gentischer H, Birke KP, Henning HM, Biro D. Electrolyte study with in operando pH tracking providing insight into the reaction mechanism of aqueous acidic Zn//MnO_2 batteries. ChemElectroChem. 2021;8(18):3553. https://doi.org/10.1002/celc.202100888.
[80] Wei TY, Li Q, Yang GZ, Wang CX. Pseudo-Zn-air and Zn-ion intercalation dual mechanisms to realize high-areal capacitance and long-life energy storage in aqueous Zn battery. Adv Energy Mater. 2019;9(34):1901480. https://doi.org/10.1002/aenm.201901480.
[81] Wahyudi W, Ladelta V, Tsetseris L, Alsabban MM, Guo XR, Yengel E, Faber H, Adilbekova B, Seitkhan A, Emwas AH, Hedhili MN, Li LJ, Tung V, Hadjichristidis N, Anthopoulos TD, Ming J. Lithium-ion desolvation induced by nitrate additives reveals new insights into high performance lithium batteries. Adv Funct Mater. 2021;31(23):2101593. https://doi.org/10.1002/adfm.202101593.
[82] Zhao K, Fan GL, Liu JD, Liu FM, Li JH, Zhou XZ, Ni YX, Yu M, Zhang YM, Su H, Liu QH, Cheng FY. Boosting the kinetics and stability of Zn anodes in aqueous electrolytes with supramolecular cyclodextrin additives. J Am Chem Soc. 2022;144(25):11129. https://doi.org/10.1021/jacs.2c00551.
[83] Pan HL, Shao YY, Yan PF, Cheng YW, Han KS, Nie ZM, Wang CM, Yang JH, Li XL, Bhattacharya P, Mueller KT, Liu J. Reversible aqueous zinc/manganese oxide energy storage from conversion reactions. Nat Energy. 2016;1(5):16039. https://doi.org/10.1038/nenergy.2016.39.